Survival of magnetic correlations above the ordering temperature in the ferromagnetically ordered classical kagome magnet $Li_9Cr_3(P_2O_7)_3(PO_4)_2$

R. Kumar,[1,*] A. Chakraborty,[2,3] S. Fukuoka,[1] F. Damay,[4] E. Kermarrec,[5] P. L. Paulose,[6,†] and Y. Ihara[1,‡]

[1]*Department of Physics, Faculty of Science, Hokkaido University, Sapporo 060-0810, Japan*

[2]*Department of Physics, Indian Institute of Technology Kanpur, India*

[3]*Institute of Physics, Johannes Gutenberg University, Mainz, Germany*

[4]*Laboratoire Léon Brillouin, Université Paris-Saclay, CNRS, CEA, CE-Saclay, F-91191 Gif-sur-Yvette, France*

[5]*Université Paris Saclay, CNRS, Laboratoire de Physique des Solides, 91405 Orsay, France*

[6]*Department of Condensed Matter Physics and Material Sciences, Tata Institute of Fundamental Research, Colaba, Mumbai 400005, India*

(Received 6 February 2023; revised 12 April 2023; accepted 13 April 2023; published 24 April 2023)

Motivated by the recent discovery of a semiclassical nematic spin liquid state in a Heisenberg kagomé antiferromagnet $Li_9Fe_3(P_2O_7)_3(PO_4)_2$ (LFPO) with $S = 5/2$ [Kermarrec *et al*. Phys. Rev. Lett. **127**, 157202 (2021)], we now investigate the impact of spin quantum number S on the ground-state properties by studying the isostructural kagomé magnet $Li_9Cr_3(P_2O_7)_3(PO_4)_2$ (LCPO) with active t_{2g} orbitals and $S = 3/2$. Thermodynamic measurements reveal that the ground-state properties of LCPO is dominated by the ferromagnetic interactions with a mean-field temperature $\Theta \sim 3$ K($J < 1$ K) and the ordering temperature, $T_c \sim 2.7$ K, and the size of the ordered moment $\sim 1.05 \pm 0.25\ \mu_B$ is significantly reduced from that of a fully ordered moment. The *ab initio* electronic structure calculations nicely corroborate the thermodynamic results and suggest the presence of additional in- and out-of-plane further-neighbor antiferromagnetic couplings, although significantly weaker in comparison to the dominant first-nearest-neighbor ferromagnetic coupling. The spin-lattice relaxation rate measured with fields larger than the saturation field shows a magnetic field induced gap ($\Delta \propto B$) in the excitation spectrum, and in $B \to 0$ limit the gap has a finite intercept ~ 3 K, equivalent to the mean-field scale. We interpret the origin of this gap is associated with the magnetic interactions inherent to the material. With our experimental results, we establish the stabilization of a ferromagnetic like ground state and the persistence of magnetic correlations above the ordering temperature in LCPO.

DOI: 10.1103/PhysRevB.107.134432

I. INTRODUCTION

The kagomé lattice with antiferromagnetic interactions has the distinction of being a highly frustrated lattice in two-dimensional (2D) that defies the Néel order and hosts a highly dynamic state of moments (spin liquid with emergent excitations) [1,2]. On the other hand, a kagomé lattice with ferromagnetic interactions does not manifest a classical/quantum spin liquid state, but rather stabilizes a purely ferromagnetic (FM) ground state [3]. Chisnell *et al.* [4] have demonstrated that the insulating kagomé ferromagnet has the potential to host topological properties such as the topological magnon bands as well as a bulk magnon Hall effect [5].

While the low-spin quantum number $S = 1/2$ based kagomé materials have been the primary choice of researchers and were thoroughly studied in quest of discovering a spin liquid state [1–3,6–8], the materials with $S > 1/2$ are relatively less explored, but at the same time are equally interesting and promising to look for some uncharted phases of quantum magnetism [9–15]. For example, be it the idea of a hexagonal-singlet solid state [9] or a resonating Affleck-Kennedy-Lieb-Tasaki loop (RAL) [16,17] state in the context of $S = 1$ kagomé Heisenberg antiferromagnet (KHAF), the appearance of magnetic field induced nematic and supernematic phases in $S = 1$ and $S = 2$ kagomé antiferromagnets [18], a highly debated ground state of a $S = 3/2$ kagomé material, $SrCr_{9p}Ga_{12-9p}O_{19}$, ranging from a spin glass, spin liquid, to a topological glass [19–26], and the presence of a one-third magnetization plateau in a $S = 5/2$ KHAF under higher magnetic fields [15], to name a few.

We have been investigating a family of kagomé materials with chemical formula $Li_9M_3(P_2O_7)_3(PO_4)_2$ [27] and recently some of us discovered a classical spin liquid state in the temperature range T_N (1.3 K) $\leqslant T \leqslant \Theta$ (11 K), and the signature of a one-third plateau in magnetization of the Fe^{3+} ($S = 5/2$) based compound $Li_9Fe_3(P_2O_7)_3(PO_4)_2$ (LFPO) [15]. The structure is highly flexible and can accommodate a variety of magnetic ions M [$= V^{3+}$ ($S = 1$), Cr^{3+}($S = 3/2$), and Fe^{3+}($S = 5/2$)] and nonmagnetic ions M [$= Al^{3+}$ and Ga^{3+}] while keeping the trigonal symmetry preserved. The material with quantum number $S = 1$, i.e., $Li_9V_3(P_2O_7)_3(PO_4)_2$ is found to exhibit the signature of ferromagnetic fluctuations in its ground state and this

*photon1900@gmail.com
†paulose@tifr.res.in
‡yihara@phys.sci.hokudai.ac.jp

material could be a potential candidate to stabilize some of the competing magnetic phases by perturbing the local energy scale [28–32]. All in all, this family offers a greater tunability to the ground-state properties on changing the orbital selection and the magnitude of spin quantum number by varying the trivalent ion, so the associated quantum fluctuations, very much like the extensively studied jarosite family of kagomé materials, but with an important difference being in the nature of their ground-state properties [33–37]. More importantly, a low exchange ($J \leqslant 1$ K) makes this family of materials the suitable candidates to realize some of the magnetic field induced novel quantum phases.

Herein, we investigate the structural and thermodynamic properties of a *structurally clean* two-dimensional kagomé material $Li_9Cr_3(P_2O_7)_3(PO_4)_2$ (LCPO) [27] by employing a number of probes including x-ray, neutron diffraction, magnetization, specific heat, and NMR. To our surprise, the kagomé network decorated with Cr^{3+} ions ($S = 3/2$) stabilizes a ferromagnetic-like ground state. In this study, we will highlight the possible reasons behind the stability of a ferromagnetic order in LCPO.

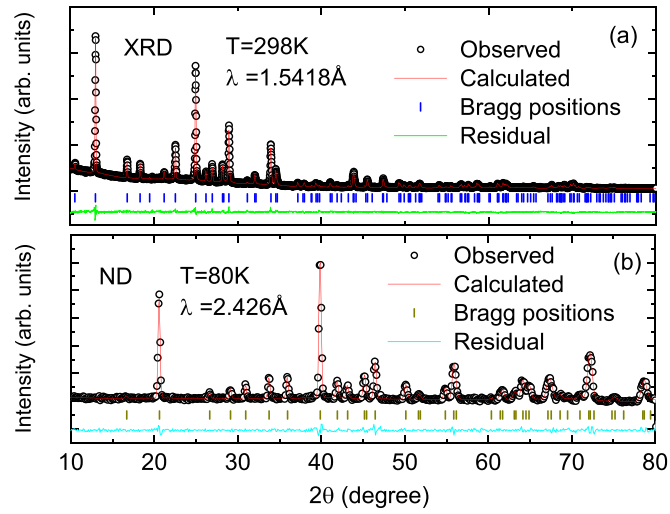

FIG. 1. (a) Powder x-ray diffraction profile of LCPO collected at $T = 298$ K with $\lambda = 1.5418$ Å. (b) Neutron diffraction profile collected at $T = 80$ K with $\lambda = 2.426$ Å.

II. EXPERIMENTAL AND THEORETICAL DETAILS

The polycrystalline samples of LCPO were synthesized by mixing and heating the materials: LiH_2PO_4 (Alfa Aeasar: 97% purity), Cr_2O_3 (Alfa Aeasar: 99.98% purity), and $Li_4P_2O_7$ in stoichiometry at different temperatures for varying duration (in hours): 250°C (6 h), 500°C (12 h), 700°C (12 h), 730°C (12 h), and 750°C (24 h) on a platinum foil in a programed Carbolite furnace. The $Li_4P_2O_7$ was prepared by baking a stoichiometric amount of Li_3PO_4 (Sigma-Aldrich: >99.9% purity) and $(NH_4)H_2PO_4$ (Sigma-Aldrich: >99.99% purity) in the temperature range 300–605°C (24h) with several intermittent grindings. The phase purity and the structural determination was carried out using the data collected on a PANalytical X'Pert PRO diffractometer at room temperature using Cu K_α radiation ($\lambda = 1.5418$ Å) and also on the neutron diffraction data (acquired on the G4.1 diffractometer at the LLB) collected in the temperature range 1.65–80 K with a wavelength $\lambda = 2.426$ Å. The dc magnetization measurements were carried out on a Quantum Design MPMS XL system and the heat capacity was measured using thermal-relaxation method in the temperature range 1.8–230 K utilizing the heat capacity option of a Quantum Design PPMS, whereas in the temperature range 0.6–10 K, a homemade calorimeter was used, and the low-temperature C_p data were scaled in the common temperature range. The ac susceptibility measurements under pressure (0–9 kbar) were done on a Quantum Design MPMS XL system using the pressure cell option from the *easylab*. NMR measurements were performed using a homemade spectrometer constructed with the software-defined radio technology [38]. For the field-sweep NMR spectrum measurements, we used a 14-T Oxford magnet energized by IPS120 power supply, which can sweep the magnetic fields at a constant rate.

The electronic structure calculations based on density functional theory (DFT) presented in this paper are carried out in the plane-wave basis within generalized gradient approximation (GGA) [39] of the Perdew-Burke-Ernzerhof exchange correlation supplemented with Hubbard U as encoded in the Vienna *ab initio* simulation package (VASP) [40,41] with projector augmented wave potentials [42,43]. The LCPO crystal consists of two formula units with a total of 98 atoms within the unit cell. The calculations are done with usual values of U and Hund's coupling (J_H) chosen for Cr with U_{eff} ($\equiv U - J_H$) $= 3.5$ eV in the Dudarev scheme [44]. In order to achieve convergence of energy eigenvalues, the kinetic energy cut off of the plane wave basis was chosen to be 500 eV. The Brillouin zone integration is performed with $4 \times 4 \times 4$ Monkhorst grid of k points.

III. RESULTS AND DISCUSSION

X-ray diffraction data collected on a polycrystalline sample of LCPO is shown in Fig. 1(a). The data were refined using FullProf Suite program [45] under the centrosymmetric space group $P\bar{3}c1$ (no. 165) and the extracted lattice parameters $a = b = 9.6654(2)$ Å and $c = 13.5904(1)$ Å are in an excellent agreement with the literature reported values [27]. The atomic position refinement using x-ray diffraction data, however, lead to the overrefined values of oxygen atomic positions, violating the Shannon ionic radii constraint [46] for P(1)-O(2) and P(2)-O(4) bonds. We then performed neutron diffraction experiments to reliably estimate the atomic positions and the neutron diffraction pattern obtained at 80 K is shown in Fig. 1(b) and the refinement results are summarized in Table I. The parameters defining the quality of experimental fit are obtained to be $R_p = 2.35\%$, $R_{wp} = 3.05\%$, $R_{\text{exp}} = 2.24\%$, and $\chi^2 = 1.85$.

Structural details. Edge sharing CrO_6 octahedra form kagomé network in *ab* plane and in a unit cell of LCPO consecutive kagomé planes are ∼6.95 Å apart and separated by nonmagnetic LiO_6 and PO_4 units, see Fig. 2(a). The kagomé lattice formed by the equilateral triangles [side ∼5 Å: forming the nearest-neighbor (nn) connectivity] has a hugely deformed kagomé hexagon with the lowest and highest angles being 89.8° and 150.2°, see Fig. 2(b), while for a regular kagomé

TABLE I. Unit-cell parameters for LCPO after neutron diffraction refinement at $T = 80$ K with ($\lambda = 2.426$ Å) and the obtained lattice constants are $a = b = 9.6492(8)$ Å and $c = 13.5654(2)$ Å.

Atoms	Site	x	y	z	Biso	Occupancy
P(1)	4*d*	2/3	1/3	0.6279(32)	0.53	1
P(2)	12*g*	0.3213(23)	0.0893(27)	0.8409(20)	0.73	1
Cr	6*f*	0.5780(61)	0.0	0.75	0.22	1
Li(1)	2*b*	0.0	0.0	0.0	1.97	1
Li(2)	4*d*	2/3	1/3	0.8639(76)	0.71	1
Li(3)	12*g*	0.3524(63)	0.1009(64)	0.0751(54)	0.91	1
O(1)	4*d*	2/3	1/3	0.5194(26)	0.71	1
O(2)	6*f*	0.2039(34)	0.0	0.75	0.77	1
O(3)	12*g*	0.6752(18)	0.1827(20)	0.6618(18)	0.63	1
O(4)	12*g*	0.4851(29)	0.1088(22)	0.8279(20)	0.71	1
O(5)	12*g*	0.3308(15)	0.2546(26)	0.8464(14)	0.27	1
O(6)	12*g*	0.2309(22)	–0.0064(20)	0.9310(15)	0.67	1

pattern, vertices in a hexagon tend to make an angle of 120.0°. Despite the kagome deformation, the structure possesses a unique magnetic site with equilateral triangles preserving the kagome physics. The magnetic interaction between Cr ions is mediated via extended pathways (Cr-O-P-O-Cr) provided by the PO_4 bridges, see Fig. 2(c). In particular, two crystallographically inequivalent phosphorus atoms—P(1) at 4*g* and P(2) at 12*d*—are responsible for facilitating the interactions between intratriangle and kagomé network. Magnetic interaction is expected to be weak in view of the extended pathways.

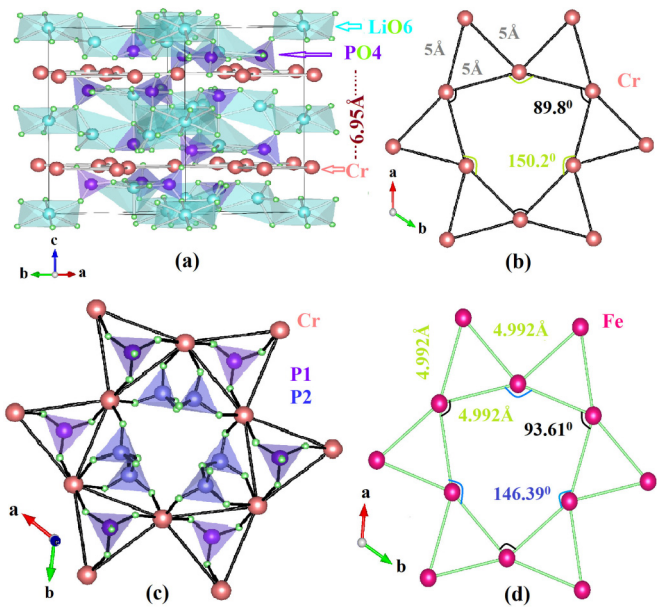

FIG. 2. The crystal structure of LCPO drawn using VESTA program [47]. (a) A representative unit cell of LCPO with kagomé layers (Cr) separated by LiO_6 octahedra (light cyan) and PO_4 tetrahedra (light violet). (b) A view of kagomé plane formed by Cr atoms in *ab* plane. (c) Interaction pathways between Cr atoms, for a kagomé motif, mediated through PO_4 bridges. (d) A view of kagomé plane formed by Fe atoms (in LFPO) in *ab* plane. [Note: P1 (violet) is located apically the center of each triangle and its position changes alternatively from z to $-z$ on moving from one to the next triangle, while P2 (light blue) is structurally positioned inside the kagomé hexagon.]

On comparing the LCPO with LFPO, it is noticeable that the distance between Fe ions forming the kagomé network is slightly reduced ∼4.992Å and also the kagomé hexagon is marginally less distorted, Fig. 2(d). Notably, the LCPO has a reduced unit cell [$a = b = 9.6654(2)$ Å, $c = 13.5904(1)$ Å, and V = 1099.536(24) Å^3] with respect to the LFPO, which has a slightly larger unit cell [$a = b = 9.7195(8)$ Å, $c = 13.6059(2)$ Å] with cell volume V = 1113.128(22) Å^3.

A. Magnetization

The temperature and field dependence of dc magnetic susceptibility ($\chi = M/H$) measured in the temperature range 1.8–300 K and field range 0.1–3 T is shown in Fig. 3(a). $\chi(T)$ shows a weak temperature dependence in a large temperature region (10–100 K) and then abruptly increases below ∼10 K, indicating a possible thermodynamic phase transition. A fit to the Curie-Weiss law, $\chi = \chi_0 + C/(T - \Theta)$, in the temperature range 10–300 K [48] results in a temperature independent

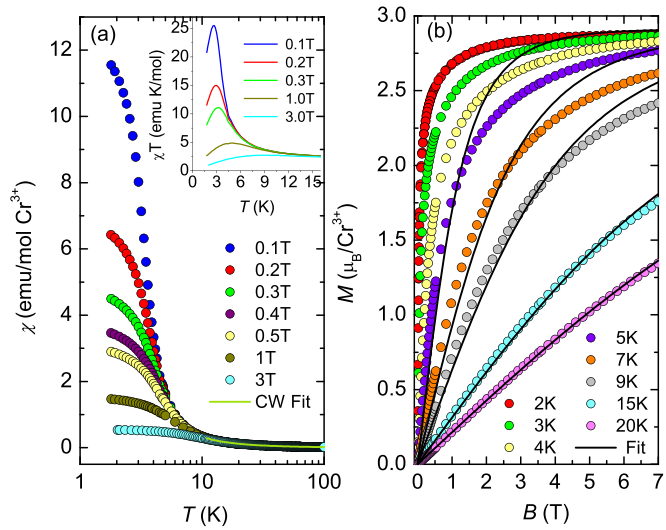

FIG. 3. (a) dc susceptibility as a function of temperature in the field range 0.1–3 T and the solid line (green) is a fit to the Curie-Weiss law. Inset: χT vs T plot. (b) Magnetic isotherms (filled circle) and their fit to the Brillouin function (black solid line) in the field range 0–7 T.

TABLE II. Fitting results of magnetic isotherm data with the Brillouin function for $g = 1.94$.

Isotherm data (K)	20	15	9	7	5
θ(K)	5.36(2)	4.97(3)	4.11(6)	3.74(6)	3.43(6)

susceptibility [$\chi_0 = (-6.6158 \pm 0.61) \times 10^{-4}$ emu/mol Cr], Curie constant [$C = 1.839(4)$ emuK/mol Cr], and Curie-Weiss temperature [$\Theta = 4.54(2)$ K]. A positive value of Θ is indicative of the fact that the predominant interaction is ferromagnetic in nature and the estimated value of paramagnetic moment, $\mu_{\text{eff}} = 3.84 \pm 0.18\ \mu_B$, is in close agreement with the spin-only moment value, $\mu_{\text{eff}} = 3.87\ \mu_B$, as expected for $S = 3/2$. The role of spin-orbit coupling is expected to be much weaker for half-filled Cr^{3+} ($t_{2g}^3 e_g^0$: $S = 3/2$; high-spin electronic configuration) and so was the case with sister material, LFPO, which has partially filled Fe^{3+}($t_{2g}^3 e_g^2$: $S = 5/2$) orbitals. Interestingly, despite having a compact unit cell, the LCPO shows a reduced Curie-Weiss temperature in comparison to LFPO ($\Theta = -11$ K), inferring the importance of markedly different exchange pathways and relative angles governing the magnetic properties. Magnetic isotherms measured in the temperature range 2–20 K [Fig. 3(b)] do not exhibit the signature of any hysteresis and the material gets nearly fully polarized ($g\mu_B S = 3\ \mu_B$) with the saturation moment $M_S = 2.91\ \mu_B$ and $g \sim 1.94$ on applying the magnetic field of strength a little over 1 T at 2 K, possibly hinting either (i) the soft nature of ferromagnetism or (ii) the presence of antiferromagnetic coupling in addition to the dominant nearest-neighbor ferromagnetic coupling. A rounded peak in the χT vs T plot [inset of Fig. 3(a)] for fields $B \leqslant 1$ T is a manifestation of the simultaneous presence of both the ferro- and antiferromagnetic interactions, which on increasing the field value gradually diminishes in magnitude and smoothly connects to the paramagnetic region. It is to be noted that for fields $B \geqslant 1$ T, the ground state gets completely polarized and the material as a whole essentially starts behaving like a polarized ferromagnet. The presence of additional couplings has nicely been captured in our electronic structure calculations (see Sec. III D) and the obtained results are in conjunction with the magnetization data.

Next, we fitted the $M(H, T)$ data to the following equation: $M(H, T) = N_A \mu_B S g B_S(gSH\mu_B/k_B(T - \theta))$, where the symbols N_A, μ_B, S, g, B_S, k_B, and θ are the Avogadro number, the Bohr magneton, spin, the spectroscopic splitting factor, the Brillouin function, the Boltzmann constant, and correlation temperature, respectively. The θ was the only free parameter in the fit and the fitting values are tabulated in Table II. The fitting of the magnetic isotherms results in an average value of $\theta \sim 4.5 \pm 0.75$ K. It is evident from Fig. 3(b) that the fitting starts deviating below 15 K, possibly highlighting the survival of magnetic correlations even above the mean-field temperature $\Theta = 4.54(2)$ K perhaps due to competing interactions.

B. Neutron diffraction

The neutron diffraction profiles were collected down to 1.65 K, shown in Fig. 4(a). The absence of extra reflections other than the nuclear Bragg peaks below T_c signifies the absence of an antiferromagnetic ordering. However, a subtle enhancement in the intensities of a fewer reflections was observed at 1.65 K compared to 5 K and 80 K and the difference profile, Fig. 4(b), makes this non-negligible increment more evident. A relatively small enhancement in the intensity of some of the Bragg peaks is compatible with a ferromagnetic model with the propagation vector $k = 0$. The representational analysis using the BasIreps option of FullProf program reveals six irreducible representations (IRrep) for the centrosymmetric trigonal space group ($P\bar{3}c1$). Of which, IRrep(5) and IRrep(6) found to generate reflections at most of the Bragg positions, but IRrep(5) was discarded as it missed out one of the most intense reflections at $\sim 20.5^\circ$. The simulated pattern with IRrep(6) is shown in Fig. 4(b) and the resultant magnetic structure is shown in Fig. 5. The data

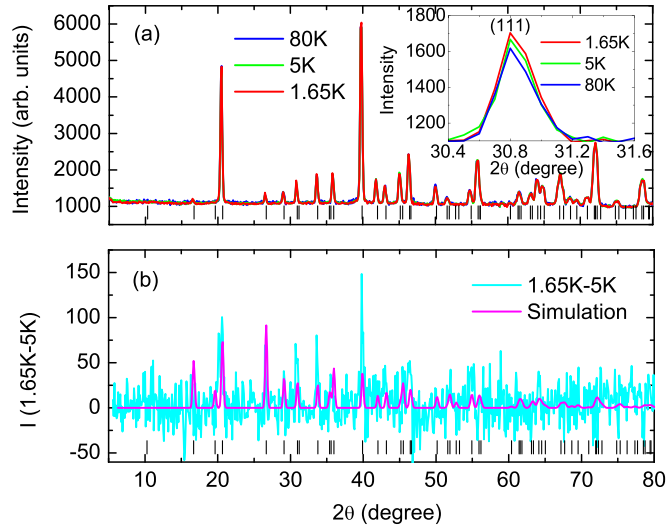

FIG. 4. (a) Neutron diffraction profiles measured at $T = 80$, 5, and 1.65 K. Inset depicts the zoomed portion of diffraction profile for the (111) Bragg peak. (b) Difference profile (cyan line) after subtracting out the 5 K data from the 1.65 K data. The pink solid line represents a simulated pattern for a ferromagnetic model with $k = 0$ and ordered moment 1.05 μ_B. The negative intensity in the vicinity of some of the Bragg positions results due to a noisy background.

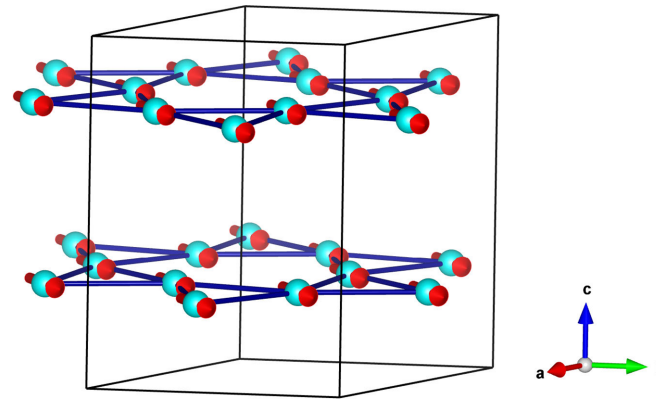

FIG. 5. A possible magnetic structure for LCPO with the resultant moment lying in the *ab* plane.

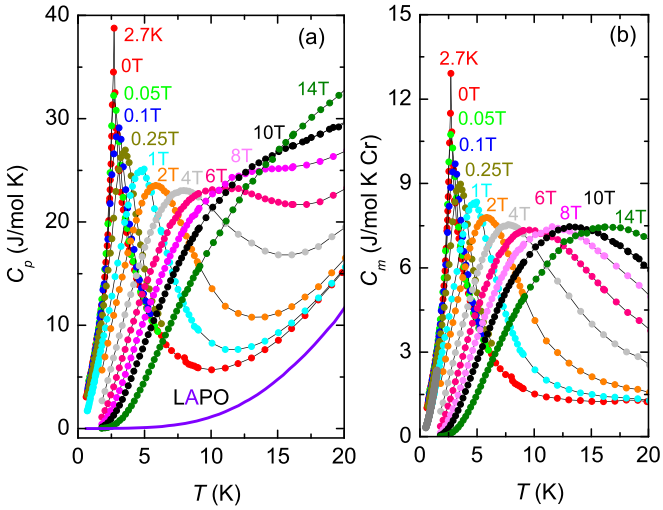

FIG. 6. (a) C_p vs T in the magnetic field range 0–14 T for LCPO and for nonmagnetic sample LAPO at $B = 0$ T. (b) Magnetic specific heat C_m after subtracting out the phononic contribution.

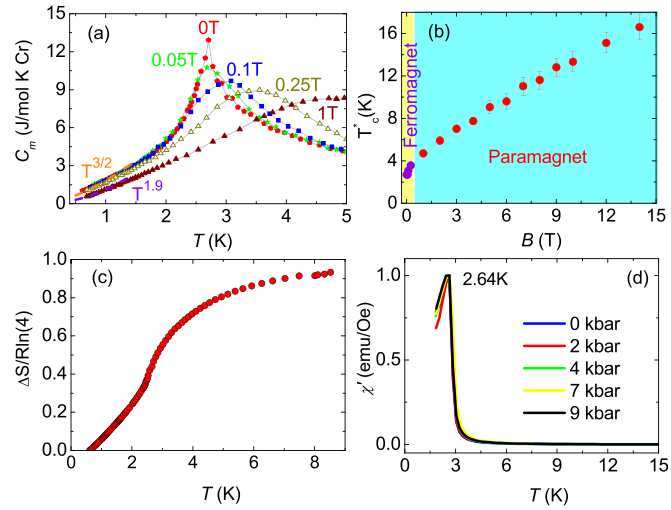

FIG. 7. (a) C_m and its fit to the equation: $C_m \propto T^{\alpha}$ for fields $0 \leqslant B \leqslant 1$ T; orange and violet dashed lines denote fit to the $T^{\frac{3}{2}}$ and $T^{1.9}$, respectively. (b) Field-induced shift in the peak position of anomaly defined by the temperature ($T_c = B \leqslant B_c$ and $T_c^* = B \geqslant B_c$). (c) Entropy change ($\triangle S$) at $B = 0$ T in the T range 0.6–10 K. (d) Real component of ac susceptibility in the pressure range 0–9 kbar. (B_c: the critical value of magnetic field required to perturb the ground state.)

statistics is neither sufficient to reliably extract the absolute size of the ordered moment (μ_{ord}) nor to discard a moderate spin canting, but our best estimate gives a value $\sim 1.05 \pm 0.25\ \mu_B$ lying in the *ab* plane. It is highly likely that the missing moment could be distributed in the inelastic or quasi-elastic channel of scattering in the form of diffuse scattering.

C. Heat Capacity

In an attempt to better understand the ground state and the nature of its excitations, we performed specific heat measurements in the temperature range 0.6–230 K and the field range 0–14 T and the results are shown in Fig. 6(a). A sharp anomaly, hallmark of a thermodynamic phase transition, was seen at 2.7 K in C_p data on measuring with zero external field. However, the anomaly was found to get broadened and gradually shifted towards higher temperature side upon stepping up the external field. The magnetic specific heat $C_m (= C_p - C_{\text{lattice}})$ was extracted after subtracting out the lattice specific heat contribution from the total specific heat C_p. An isostructural nonmagnetic material $Li_9Al_3(P_2O_7)_3(PO_4)_2$ (LAPO) was measured for estimating the C_{lattice} and its Debye temperature was renormalized in accordance with the magnetic material by employing the Bouvier scaling [49]. As shown in Figs. 6(b) and 7(a), the transition temperature $T_c (\sim 2.7$ K) remains field invariant in the narrow field range 0–0.05 T, but the anomaly shifts towards higher temperatures and also gets broadened on increasing the magnetic field from 0 to 14 T. Such a field-induced elevation of the transition temperature is akin to the Schottky behavior and is a typical signature for a ferromagnetic system, as for an antiferromagnet the transition temperature gets pushed down to the lower temperatures on increasing the field strength. A gradual reduction in the Schottky's peak amplitude with the applied magnetic field until $B \geqslant 8$ T is also apparent from Fig. 6(b). The field-dependent variation of the peak shift is shown in Fig. 7(b) and it is apparent that for fields ($B \geqslant 0.25$ T) the peak temperature, labeled as T_c^*, linearly scales with the external field strength, suggesting that the Zeeman energy scale becomes comparable to the exchange coupling (J) for $B \geqslant 0.25$ T, thus above this field the ground state essentially starts deviating from a true ferromagnet and transforms into a partially polarized state. In view of the observed magnetic ordering temperature (2.7 K), we also calculated the strength of magnetic dipole interaction term ($\sim \mu^2/4\pi r^3$) and the obtained value of dipolar energy scale ($E_{\text{dip}}/k_B \sim 0.04$ K) was found to be two orders of magnitude lower than the ordering temperature, which clearly means that the magnetic ordering is mainly dominated by the exchange interactions.

In the framework of spin wave theory, for a dispersion of the type: $\omega \propto k^{\phi}$, the magnetic specific heat is shown to have a temperature dependence of the form: $C_m \propto T^{\alpha}$; $\alpha = \frac{d}{\phi}$, where d and ϕ are the magnetic dimensionality of lattice and exponent in dispersion relation, respectively. The C_m was found to have a $T^{1.3}$ dependence (not shown) in the temperature range 1.5–0.6 K at $B = 0$ T and retains the same dependence in the field range 0–0.1 T. The obtained temperature dependence of C_m is very close to the expected $\sim T^{\frac{3}{2}}$ behavior (anticipated for a 3D ferromagnet) [50], see Fig. 7(a). According to the Mermin-Wagner theorem [51], a long-range magnetic order (LRO) can not be realized in the 2D isotropic Heisenberg model at $T > 0$ K because of the long-range magnetic fluctuations, and therefore a finite 3D coupling between the kagome layers is required to uphold a magnetic transition at $T > 0$ K. On the other hand, for $B = 1$ T, C_m varies as $\sim T^{1.9}$, which reflects the field-induced perturbation in the excitation spectrum. The magnetic entropy change estimated in the temperature range 0.6 and 10 K yields $\sim 95\%$ of $R\ln(4)$, expected for $S = 3/2$, see Fig. 7(c). In fact, the recovery of $\gtrsim 35\%$ entropy above the mean-field temperature commensurate with the magnetic-isotherm

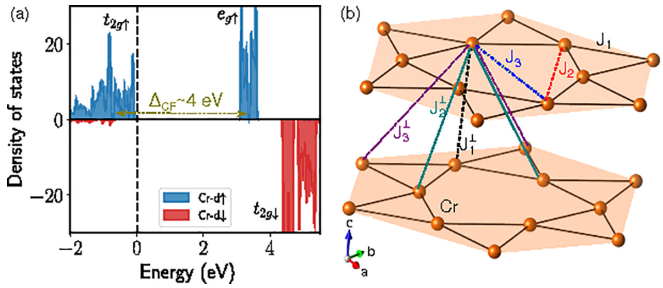

FIG. 8. (a) Orbital resolved spin-polarized density of states plot of Cr-*d* orbitals within GGA + U calculations. (b) First-, second-, and third-neighbor intraplanar (J_1, J_2, and J_3) and interplanar ($J_1^\perp$, $J_2^\perp$, and $J_3^\perp$) exchange interaction paths.

analysis and further signifies the persistence of magnetic correlations. The survival of magnetic correlations above Θ was also seen in a $S = 3/2$ quasi-2D honeycomb material $Ag_3LiMn_2O_6$ [52].

ac-susceptibility measurements were performed under pressure with an intention of exploring the possibility of a pressure induced criticality. The real component of ac susceptibility measured ($H_{ac} = 1$ Oe, $f = 11$ Hz, $H_{dc} = 0$) in the pressure range 0–9 kbar is shown in Fig. 7(d). However, no appreciable change in the transition temperature ~2.64(10) K was observed and the transition was found to be robust in the measured pressure range.

D. Electronic structure calculation

To corroborate the experimental findings with theoretical calculations, we have performed spin-polarized GGA + U calculations with a ferromagnetic (FM) arrangement of Cr spins. The local octahedral environment splits the Cr-*d* orbitals into low lying t_{2g} triplets and higher energy e_g doublets maintaining a crystal field splitting of ~4.0 eV. The plot of spin-polarized density of states in Fig. 8(a) reveals that the majority channel of the Cr-t_{2g} levels are completely filled with three valence electrons and the minority channel of t_{2g} and the e_g orbitals are completely empty. Within the FM calculation, the total moment per formula unit, containing six Cr atoms, is calculated to be 18.0 μ_B, which further supports the 3+ charge state of Cr and is also consistent with the experimental value of effective moment($\mu_{eff} = 3.84$ μ_B). FM calculation gives the magnetic moment per Cr site to be 2.90 μ_B, as the rest of the moment lies in the ligand sites (0.01μ_B/O). Inclusion of spin-orbit coupling (SOC) in our calculation only lowers the energy of FM state further by 74 meV keeping the moment value per Cr similar to that of without SOC calculations. The small value of orbital moments [m_l(Cr) = 0.04 μ_B] in GGA + SOC + U calculations suggests SOC acts perturbative ($m_l/m_s \sim 0.01$) in the system and has negligible impact on stabilizing the ground state.

In order to understand the magnetic exchange interactions among the large intrinsic Cr spins and for a quantitative estimation of the Cr-Cr exchange couplings, we have calculated the symmetric exchange interactions (J) by mapping the total energies of several spin configurations to the Heisenberg spin model $\mathcal{H}_{sym} = J_{ij}\boldsymbol{S_i} \cdot \boldsymbol{S_j}$ [52]. Our calculations suggest that the nearest-neighbor (nn) interaction is ferromagnetic in nature with exchange strength $J_1 = 0.22$ meV. The obtained further neighbor in-plane and out-of-plane couplings [see Fig. 8(b) for connectivity] are antiferromagnetic in nature with magnitudes $J_1^\perp = 0.06$ meV, $J_2 = 0.03$ meV, $J_2^\perp = 0.05$ meV, $J_3 = 0.06$ meV, and $J_3^\perp = 0.03$ meV, respectively. Due to large super-exchange paths, the interaction strengths are relatively small, which is also presumed from the sufficiently low value of experimental Curie-Weiss temperature [$\Theta_{CW}^{Bulk} \sim 4.54(2)$ K or $\Theta_{CW}^{NMR} \sim 2.88(11)$ K]. Clearly, the FM exchange interaction J_1, corresponding to the nn super-exchange coupling, dominates over the further-neighbor antiferromagnetic couplings. To explore the possibility of spin canting in the system, we have also considered the antisymmetric part of the spin Hamiltonian $\mathcal{H}_{asy} = \sum_{ij} \boldsymbol{D}_{ij} \cdot (\boldsymbol{S}_i \times \boldsymbol{S}_j)$, where $\boldsymbol{D}$ is the Dzyaloshinskii-Moriya (DM) interaction parameter [53]. The calculated values of nn DM interaction is of the order of $\sim 10^{-3}$ meV. A small value of SOC strength results in the suppressed value of DM parameter. Taken together the nn FM interaction with a number of AFM interactions and small antisymmetric DM interaction, the calculated value of $\Theta_{CW} \sim 0.3$ K, which is reasonably small and further affirms a ferromagnetic ground state. However, it must be noted that the calculated value of Θ_{CW} depends on the chosen exchange configuration and could vary between ~0.3(Θ_{CW}^{min} : summing up all the J's) and 12 K (Θ_{CW}^{max} : only nearest neighbor). Apparently, the experimentally estimated value of Θ_{CW}^{NMR}~2.88(11) K is less than the computed value of Θ_{CW}^{max}~12 K, implying the relevance of additional antiferromagnetic couplings beyond the nearest-neighbor ferromagnetic coupling ($J_1 = 0.22$ meV). Meisso *et al.* [54] sketched a phase diagram based on the lattice symmetries of a perfect kagomé lattice for the identification of a most probable ground state in a large parameter space of Heisenberg model with the intra-planar kagomé couplings J_1-J_2-J_3-$J_3^\perp$, which suggests the stabilization of a rather complex ground state for LCPO and places it in the proximity of a ferromagnetic and spiral state. Nevertheless, in view of the skewed C_6 symmetry with additional interlayer couplings (as is the case with LCPO) the fate of the ground-state selection is beyond the purview of the present model and calls for further investigations.

E. NMR Spectroscopy

The LCPO offers two potential NMR sensitive nuclei, ^{7}Li($I = 3/2$ and $\frac{\gamma}{2\pi} = 16.546$ MHz/T) and ^{31}P($I = 1/2$ and $\frac{\gamma}{2\pi} = 17.235$ MHz/T) to probe the magnetism ensuing from the kagomé network formed by the Cr^{3+} ions. ^{7}Li was found to be poorly coupled to the kagomé network because of a weak hyperfine coupling, resulting from the relatively extended pathways. We then switched to ^{31}P-NMR to probe the static susceptibility and relaxation rate measurements. LCPO being a low-J (<1 K) material with a small saturation field ~1 T, it was challenging [55] to address the ground-state properties of the material by employing NMR as a probe for magnetic fields comparable to the energy scale set by the exchange coupling. In lieu of that we investigated the effect of magnetic field on the ground-state properties for $B \geqslant 3$ T. The ^{31}P-NMR spectra were collected at fixed frequencies ($f = 51.50$ MHz, 120.51 MHz, and 215.50 MHz) by sweep-

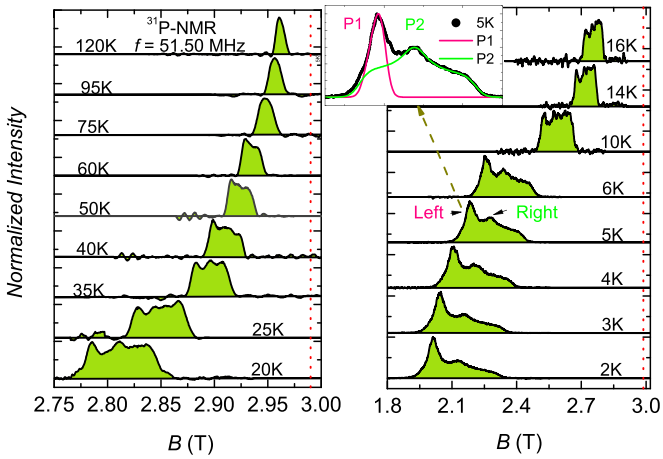

FIG. 9. ^{31}P-NMR spectra measured at NMR frequency $f =$ 51.50 MHz. Vertical dashed line depicts the ^{31}P-NMR reference field. The peaks marked with "Left" and "Right" are originating from two different phosphorous sites P(1) and P(2), see text. Inset: ^{31}P-NMR spectrum at 5 K fitted with two NMR lines; P1 (left peak) and P2 (right peak).

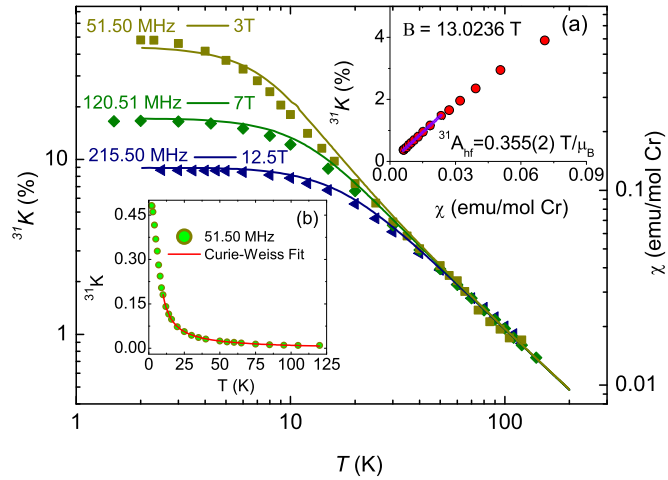

FIG. 10. Temperature dependence of ^{31}P-NMR line shift (symbols) measured at three different NMR frequencies: $f = 51.50$ MHz (3 T), 120.51 MHz (7 T), and 215.50 MHz (12.5 T) (left y axis) for line P1. Variation of bulk susceptibility (lines) with temperature measured at 3 T, 7 T, and 12.5 T (right y axis). Insets: (a) K - χ plot for line P1, and (b) ^{31}P-NMR line shift (filled circle) measured at $f = 51.50$ MHz and the line (red) is a fit to the Curie-Weiss type equation, described in text.

ing the magnetic field using the Hahn echo. Figure 9 shows the ^{31}P-NMR spectra measured in the temperature range 120–2 K for the NMR frequency $f = 51.50$ MHz. Structurally there are two distinct P sites, P(1) and P(2), in a unit cell of LCPO with the Wyckoff positions 4g (2/3, 1/3, z) and 12d (x, y, z) respectively, but in the T range 120–75 K, we observed only one ^{31}P-NMR line with a nearly Gaussian line-shape because the other ^{31}P-NMR line was also buried under the same line as a result of having a nearly similar NMR shift [55]. Upon further lowering the temperature, the ^{31}P-NMR line shape starts developing structure and progressively becomes highly asymmetric; nevertheless below about 10 K the spectral shape can largely be interpreted as a superposition of two NMR lines: *Left* line and *Right* line, see Fig. 9. As evident from Fig. 2, phosphorus atoms located at the sites: 4g, i.e., P(1), and 12d, i.e., P(2), are coupled to three and two Cr atoms, respectively, therefore ^{31}P-NMR signal corresponding to P(1) is expected to be shifted more in comparison to P(2) with respect to the NMR reference line, and also the ^{31}P-NMR spectrum arising from P(1) is anticipated to be less anisotropic in comparison to P(2) as a result of being situated at a more symmetric position in the unit cell. Owing to their atomic weight percentage (4 : 12) in a unit cell of LCPO, both P(1) and P(2) are expected to maintain an intensity ratio of 1 : 3 in ^{31}P-NMR spectrum. With this notion, we chose a spectrum collected at 5 K (inset of Fig. 9) and the ^{31}P-NMR shift was fitted using Eq. (1) and the obtained results are summarized in Table III.

$$K = K_{\rm iso} + K_{ax}(3\cos^2\theta - 1) + K_{\rm ani}\sin^2\theta\cos 2\phi \qquad (1)$$

where $K_{\rm iso}$, K_{ax}, and $K_{\rm ani}$ are the isotropic, axial, and anisotropic components of the Knight shift, respectively. While θ and ϕ are spherical polar angles defining the orientation of B with respect to the shift tensor axes.

As can be seen from the inset of Fig. 9 and the tabulated results, the *Left* peak (P1) is nearly a Gaussian, less anisotropic ($K_{\rm ani} \simeq 0\%$) in nature (as P1 is located at the three-fold axis of rotational symmetry), while the *Right* peak (P2) of the spectrum is extremely broadened, highly anisotropic ($K_{\rm ani} = 4.3\%$) and the ratio of calculated integrated intensity for P1 and P2 is in excellent agreement with the expected ratio $\sim$1 : 3.

Based on the fitting results, in line with the underlying presumptions, we can unambiguously assign the *Left* peak of ^{31}P-NMR spectrum to be originating from the phosphorus P(1) (shown by line P1) and the *Right* peak from the phosphorus P(2) (shown by line P2).

It was not possible to isolate the contributions of two peaks from the observed NMR line and thus the deduction of isotropic ($K_{\rm iso}$) and anisotropic ($K_{\rm ani}$) NMR shifts in the paramagnetic region, so we plotted the Knight shift (K) for peak P1 by taking the peak position. Figure 10 shows the ^{31}P-NMR shift (K), for P1, as a function of temperature in

TABLE III. Fitting parameters for ^{31}P-NMR spectrum collected at 5 K.

Line	$K_{\rm iso}$(%)	$K_{\rm ani}$(%)	K_{ax}(%)	Width (kHz)	Area (arb. units)	Ratio
P1	36.86	$\simeq 0$	0.93	300.05	0.038	1
P2	30.97	4.3	4.2	661.05	0.116	3.05

the T range 1.5–120 K at three different NMR frequencies. The NMR shift measurements provide a way to extract the intrinsic susceptibility (free from extraneous contributions) through the relation: $^{31}K = K_0 + (A_{\rm hf}/N_A\mu_B)\chi_{\rm local}$, where K_0, $A_{\rm hf}$, and $\chi_{\rm local}$ are the temperature independent chemical shift, hyperfine-coupling constant, and the local spin susceptibility, respectively. As evident from Fig. 10, the NMR shift (^{31}K) nicely follows the bulk susceptibility in the entire temperature range, therefore confirming the intrinsic nature of powder susceptibility data and its variation with external magnetic field. The suppression of bulk susceptibility/NMR shift as a function of magnetic field is in accordance with the magnetic isotherm data. The hyperfine coupling constant ($A_{\rm hf}$) was determined for P(1) by measuring the shift at the center position with a fixed field ($B = 13.0236$ T) and estimated to be 0.355(2) T/μ_B, shown in the inset (a) of Fig. 10. Fitting the shift (^{31}K) obtained at 51.50 MHz to the Curie-Weiss law [$^{31}K = K_0 + C/(T\text{-}\Theta)$] yields a more refined value of $\Theta = 2.88(11)$ K or $J = 3\Theta/4S(S+1) \sim 0.6$ K (compared to bulk susceptibility) with $K_0 = -0.0037(4)$, and $C = 1.32(2)$ K, see inset (b) of Fig. 10. The offset (∼1.5 K) in the value of Θ determined from the bulk susceptibility and NMR results could be the upshot of some extrinsic contributions affecting the paramagnetic behavior of bulk magnetization. As the ordering temperature $T_c = 2.7$ K (determined from the C_p data), and the mean-field temperature $\Theta = 2.88(11)$ K (from the ^{31}P-NMR line shift), are nearly the same, implying that frustration plays no role in selecting the ground state.

Now we focus our attention to understand the effect of magnetic field on the spin dynamics and for that purpose the spin-lattice relaxation rate ($1/T_1$) measurements were performed by employing the saturation recovery method at the peak position of line P1, *Left* peak of ^{31}P-NMR spectrum, in the T range 1.5–130 K and at three NMR frequencies: $f = 51.50$ MHz (3 T), 120.51 MHz (7 T), and 215.50 MHz (12.5 T). The saturation recovery data were fitted to the equation: $M_z(t) = M_0(1 - Ae^{-t/T_1})$ and the extracted values of spin-lattice relaxation rates ($1/T_1$) are plotted against temperature (T), see Fig. 11(a).

$1/T_1$ shows a marked frequency dependence even in the paramagnetic regime ($T \gg \Theta_{\rm CW}$). For the lowest frequency $f = 51.50$ MHz, it attains a maximum value ∼8 (msec)$^{-1}$ at 100 K and for the higher frequencies it reduces in a nonlinear fashion in the paramagnetic region, see Fig. 11(a). In the high-temperature region, where the ^{31}P-NMR nuclear relaxation is supposed to be dominated by the fluctuations of the localized moments of the chromium ions, $1/T_1$ can be estimated using the Moriya relation [56]: $1/T_1|_{\rm Moriya} = (2\pi)^{1/2}(A_{\rm hf}/\hbar)^2 Z_1 S(S+1)/3\omega_{ex}$; and $\omega_{ex} = (6k_B^2\Theta^2/Z_2 S(S+1)\hbar^2)^{1/2}$, where $A_{\rm hf}$, Z_1, ω_{ex}, $\Theta_{\rm CW}$, and Z_2 are hyperfine coupling constant, number of magnetic ions connected to nuclei being probed, exchange frequency, Curie-Weiss temperature, and immediate neighbors of a magnetic ion, respectively. The calculated Moriya limit $1/T_1|_{\rm Moriya}$ for both the peaks P1 and P2 is tabulated in Table IV and the relaxation rate obtained for P1 (at $f = 51.50$ MHz and $T = 100$ K) is seemingly very close to the Moriya limit, see Fig. 11(a). On the other hand, a field induced reduction of $1/T_1$ seen above 20 K($\gg \Theta_{\rm CW}$) is most likely

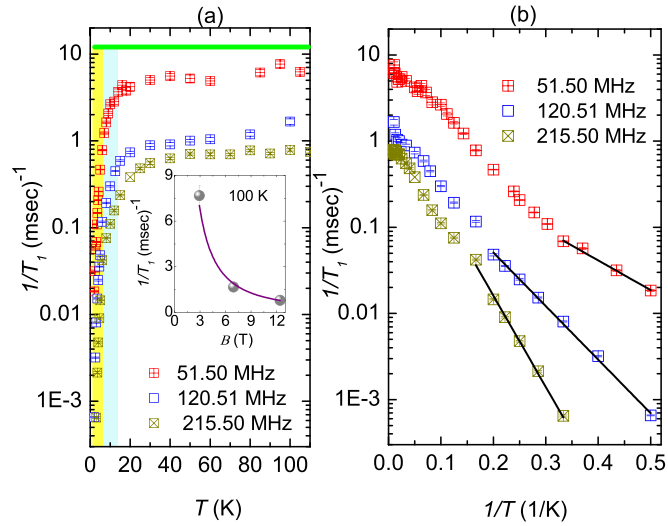

FIG. 11. Spin-lattice relaxation rate ($1/T_1$) measured at the peak position of the P1 NMR line at three different fields. (a) Semi-log plot of $1/T_1$ vs T with the Moriya limit shown by the horizontal green line. Inset shows the field variation of $1/T_1$ (grey sphere) at $T = 100$ K and the line (purple) is a fit to the power law: $1/T_1 \propto B^{-n}$. (b) $1/T_1$ vs $1/T$ in log-log scale; black solid lines are the fits to a function (see text).

occurring due to a relaxation mechanism, which involves the participation of lattice vibrational modes; a similar trend was also noticed in the $1/T_1$ behavior of sister material LFPO [15]. Inset of Fig. 11(a) depicts the variation of $1/T_1$ with applied field at $T = 100$ K and a fit to the expression: $1/T_1 = AB^{-n}$ outputs in a good fit with $n = 1.5(1)$. Such kind of relaxation behavior [57] is governed by the direct process, $n = 2$ (non-Kramers ion) and 4 (Kramers ion), and has been discussed in the context of rare-earth salts at low temperatures with a possible extension to $3d$ material, but its relevance in the high-temperature limit is questionable.

Now, we focus to understand the low-T behavior of $1/T_1$. $1/T_1$ in polarized or partially polarized state of a magnet is expected to have a gapped behavior. $1/T_1$ data fitted to an equation of the Arrhenius form: $1/T_1 = A\exp(-\Delta_N/k_BT)$ yields a gap, Δ_N (T range: ∼1.5–3 K for 3 T and ∼1.5–6.5 K for 7 and 12.5 T), see Fig. 11(b).

In order to gain more insight about the nature and origin of this gap, we further analyzed the specific heat data by modeling the Schottky anomaly (Fig. 12) and compared the results with gap obtained using NMR data, shown in Fig. 13.

In paramagnetic region and under nonzero external magnetic field ($B \neq 0$), a $S = 3/2$ system would have equally spaced $(2S+1) = 4$ energy levels with the lowest and highest energies being 0 and 3Δ, respectively, shown in Fig. 13. The

TABLE IV. Parameters used in estimating the spin-lattice relaxation rate $1/T_1|_{\rm Moriya}$ using the Moriya relation.

Z_1	Z_2	$\Theta_{\rm CW}$ (K)	g	$1/T_1\|_{\rm Moriya}$ (msec)$^{-1}$	Peak
3	4	3	1.94	11.60	P1
2	4	3	1.94	∼13.0	P2

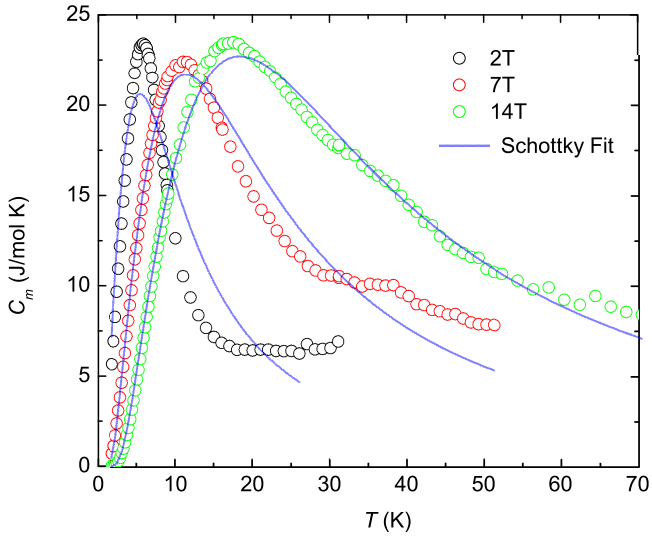

FIG. 12. Temperature dependence of magnetic specific heat (open circle) and its fitting (solid line) to the four-level Schottky system at the selected magnetic fields.

magnetic specific heat C_m was fitted to a four level system with the following expression [58]:

$$C_m = \frac{R}{k_B^2 T^2}\left[\frac{\sum_{i=0}^{3}\epsilon_i^2 e^{-(\epsilon_i/k_B T)}}{\sum_{i=0}^{3} e^{-(\epsilon_i/k_B T)}} - \left\{\frac{\sum_{i=0}^{3}\epsilon_i e^{-(\epsilon_i/k_B T)}}{\sum_{i=0}^{3} e^{-(\epsilon_i/k_B T)}}\right\}^2\right],$$

where ϵ_i denotes the energy of ith spin level and the gap is defined as $\Delta_i = \epsilon_i - \epsilon_0$ and the other notations have their usual meanings.

The Schottky fitting deviates from the experimental data below 7 T and results in a rather poor fit at 2 T, see Fig. 12. This result is suggesting that a gradual reduction observed in the Schottky peak as a function of field, Fig. 6(b), is a consequence of magnetic correlations, which persist above the mean-field temperature. The Schottky gap Δ_S estimated by modeling the magnetic specific heat data not only nicely coincides with the NMR gap (Δ_N) in a wider field range (deviates slightly at the higher fields [59]), but also linearly scales with the external magnetic field, and in $B \to 0$ limit both the gaps (Δ_S and Δ_N) attain a nonzero value of intercept ~4.1(1) K and 2.8(5) K, respectively, see Fig. 13. Apparently, the gap size estimated using these two techniques: bulk (specific heat) and local (^{31}P-NMR) probes is quite consistent and we believe that the gap size estimated using NMR is much more precise as the NMR transitions are constrained by the selection rules ($\Delta m = 1$) imposed by the magnetic dipole transitions, on the contrary, the specific heat yields an average value of gap, therefore it sets an upper bound to the gap size. Interestingly, the gap Δ_N estimated by NMR technique in $B \to 0$ limit has an intercept value close to the mean-field temperature scale ~2.88 K, which essentially implies the size of the internal field developed as a result of magnetic ordering. For fields above $B \gtrsim 3$ T, the external field takes over and the gap scales linearly with the applied field.

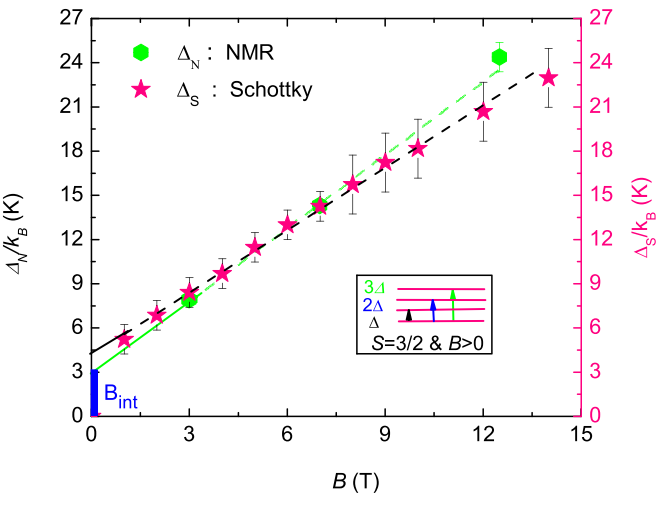

FIG. 13. Field dependence of gaps estimated using NMR [left y axis: (Δ_N/k_B)] and specific heat [right y axis: (Δ_S/k_B)] data. A schematic of the Zeeman splitting scheme for $S = 3/2$ in paramagnetic region is also shown. The green (NMR) and black (Schottky) dashed lines are fits to a straight line and the vertical thick line (blue) depicts the size of internal field.

IV. CONCLUSIONS

In summary, we have investigated the structural and physical properties of a kagomé material LCPO using x-ray diffraction and neutron diffraction, thermodynamic, and ^{31}P-NMR measurements. Even though LCPO is isostructural to LFPO, the ground state of LCPO is in stark contrast to LFPO and does not show the effect of frustration (offered by the kagomé network) and relatively stronger quantum fluctuations than LFPO as a result of reduced spin quantum number $S = 3/2$. The LCPO stabilizes a ferromagnetic like ground state with $T_c = 2.7$ K, and the short-range correlations are found to survive above the mean-field temperature Θ_{CW}~3 K. The presence of additional couplings (2nd and 3rd) turn the material away from a pure nearest Heisenberg kagomé ferromagnet. This structurally clean kagomé material is quite a rare example of an insulating ferromagnet, where the ferromagnetism is a spin-off of nn exchange interaction rather than the DM and dipolar interactions. The presence of highly degenerate flat bands in kagome lattice makes it conducive to hold the ferromagnetic state and the absence of DM interaction in LCPO could again protect the degeneracy of flat bands and thus the zero-energy excitations. In order to understand the role of these bands on the elementary excitations and in turn on the ground state, inelastic neutron scattering experiments could be of paramount importance.

ACKNOWLEDGMENTS

R.K. thanks TIFR Mumbai for facilitating with the experimental facilities for conducting the initial research work. A.C. acknowledges Indian Institute of Technology, Kanpur and Science and Engineering Research Board (SERB) National Postdoctoral Fellowship (Grant No. PDF/2021/000346), India for financial support. P.L. thanks Sudhindra Rayaprol for conducting initial neutron diffraction measurements. We thank CC-IITK for providing the high performance computing

facility. This work is partly supported by the JSPS Grant-in Aid for Scientific Research (Grants No. 19H01832, No. 21H01035, and No. 22H04458) and the ISSP Institutional Collaborative Research Program.

[1] L. Balents, Nature (London) **464**, 199 (2010).
[2] B. Bauer, L. Cincio, B. P. Keller, M. Dolfi, G. Vidal, S. Trebst, and A. Ludwig, Nat. Commun. **5**, 5137 (2014).
[3] D. Boldrin, B. Fåk, M. Enderle, S. Bieri, J. Ollivier, S. Rols, P. Manuel, and A. S. Wills, Phys. Rev. B **91**, 220408(R) (2015).
[4] R. Chisnell, J. S. Helton, D. E. Freedman, D. K. Singh, R. I. Bewley, D. G. Nocera, and Y. S. Lee, Phys. Rev. Lett. **115**, 147201 (2015).
[5] M. Hirschberger, R. Chisnell, Y. S. Lee, and N. P. Ong, Phys. Rev. Lett. **115**, 106603 (2015).
[6] J. S. Helton, K. Matan, M. P. Shores, E. A. Nytko, B. M. Bartlett, Y. Yoshida, Y. Takano, A. Suslov, Y. Qiu, J.-H. Chung, D. G. Nocera, and Y. S. Lee, Phys. Rev. Lett. **98**, 107204 (2007).
[7] T.-H. Han, J. S. Helton, S. Chu, D. G. Nocera, J. A. Rodriguez-Rivera, C. Broholm, and Y. S. Lee, Nature (London) **492**, 406 (2012).
[8] M. R. Norman, Rev. Mod. Phys. **88**, 041002 (2016).
[9] K. Hida, J. Phys. Soc. Jpn. **69**, 4003 (2000).
[10] O. Götze, D. J. J. Farnell, R. F. Bishop, P. H. Y. Li, and J. Richter, Phys. Rev. B **84**, 224428 (2011).
[11] W. Li, A. Weichselbaum, J. V. Delft, and H.-H. Tu, Phys. Rev. B **91**, 224414 (2015).
[12] H. Nakano and T. Sakai, J. Phys. Soc. Jpn. **84**, 063705 (2015).
[13] T. Liu, W. Li, and G. Su, Phys. Rev. E **94**, 032114 (2016).
[14] A. Paul, C.-M. Chung, T. Birol, and H. J. Changlani, Phys. Rev. Lett. **124**, 167203 (2020).
[15] E. Kermarrec, R. Kumar, G. Bernard, R. Hénaff, P. Mendels, F. Bert, P. L. Paulose, B. K. Hazra, and B. Koteswararao, Phys. Rev. Lett. **127**, 157202 (2021).
[16] H. Yao, L. Fu, and X.-L. Qi, arXiv:1012.4470.
[17] W. Li, S. Yang, M. Cheng, Z.-X. Liu, and H.-H. Tu, Phys. Rev. B**89**, 174411 (2014).
[18] T. Picot and D.Poilblanc, Phys. Rev. B **91**, 064415 (2015).
[19] A. P. Ramirez, G. P. Espinosa, and A. S. Cooper, Phys. Rev. Lett. **64**, 2070 (1990).
[20] B. Martínez, F. Sandiumenge, A. Rouco, A. Labarta, J. Rodríguez-Carvajal, M. Tovar, M. T. Causa, S. Galí, and X. Obradors, Phys. Rev. B **46**, 10786 (1992).
[21] A. Keren, Y. J. Uemura, G. Luke, P. Mendels, M. Mekata, and T. Asano, Phys. Rev. Lett. **84**, 3450 (2000).
[22] A. P. Ramirez, B. Hessen, and M. Winklemann, Phys. Rev. Lett. **84**, 2957 (2000).
[23] D. Bono, L. Limot, and P. Mendels, Low Temp. Phys. **31**, 704 (2005).
[24] S.-H. Lee, C. Broholm, G. Aeppli, A. P. Ramirez, T. G. Perring, C. J. Carlile, M. Adams, T. J. L. Jones, and B. Hessen, Europhys. Lett. **35**, 127 (1996).
[25] I. Klich, S.-H. Lee, and K. Iida, Nat. Commun. **5**, 3497 (2014).
[26] J. Yang, A. Samarakoon, S. Dissanayake, H. Ueda, I. Klicha, K. Iida, D. Pajerowski, N. P. Butch, Q. Huang, J. R. D. Copley, and S.-H. Lee, Proc. Natl. Acad. Sci. **112**, 11519 (2015).
[27] S. Poisson, F. d'Yoire, N. Guyen-Huy-Dung, E. Bretey, and P. Berthet, J. Solid State Chem. **138**, 32 (1998).
[28] Q. Kuang, J. Xu, Y. Zhao, C. Chen, and L. Chen, Electrochim. Acta **56**, 2201 (2011).
[29] M. Onoda and M. Inagaki, J. Phys. Soc. Jpn. **80**, 084801 (2011).
[30] M. Onoda and S. Ikeda, J. Phys. Soc. Jpn. **82**, 074801 (2013).
[31] M. Onoda and S. Ikeda, J. Phys. Soc. Jpn. **88**, 034709 (2019).
[32] M. Onoda and S. Takada, J. Phys. Soc. Jpn. **89**, 034002 (2020).
[33] D. Grohol, Q. Huang, B. H. Toby, J. W. Lynn, Y. S. Lee, and D. G. Nocera, Phys. Rev. B **68**, 094404 (2003).
[34] A. S. Wills, A. Harrison, C. Ritter, and R. I. Smith, Phys. Rev. B **61**, 6156 (2000).
[35] A. Keren, K. Kojima, L. P. Le, G. M. Luke, W. D. Wu, Y. J. Uemura, M. Takano, H. Dabkowska, and M. J. P. Gingras, Phys. Rev. B **53**, 6451 (1996).
[36] K. Matan, D. Grohol, D. G. Nocera, T. Yildirim, A. B. Harris, S. H. Lee, S. E. Nagler, and Y. S. Lee, Phys. Rev. Lett. **96**, 247201 (2006).
[37] S. Okubo, R. Nakata, S. Ikeda, N. Takahashi, T. Sakurai, W.-M. Zhang, H. Ohta, T. Shimokawa, T. Sakai, K. Okuta, S. Hara, and H. Sato, J. Phys. Soc. Jpn. **86**, 024703 (2017).
[38] Y. Ihara, K. Hayashi, T. Kanda, K. Matsui, K. Kindo, and Y. Kohama, Rev. Sci. Instr. **92**, 114709 (2021).
[39] J. P. Perdew, K. Burke, and M. Ernzerhof, Phys. Rev. Lett. **77**, 3865 (1996).
[40] G. Kresse and J. Hafner, Phys. Rev. B **47**, 558 (1993).
[41] G. Kresse and J. Furthmüller, Phys. Rev. B **54**, 11169 (1996).
[42] P. E. Blöchl, Phys. Rev. B **50**, 17953 (1994).
[43] G. Kresse and D. Joubert, Phys. Rev. B **59**, 1758 (1999).
[44] S. L. Dudarev, G. A. Botton, S. Y. Savrasov, C. J. Humphreys, and A. P. Sutton, Phys. Rev. B **57**, 1505 (1998).
[45] J. Rodríguez-Carvajal, Phys. B: Condens. Matter **192**, 55 (1993).
[46] R. D. Shannon, Acta Cryst A **32**, 751 (1976).
[47] K. Momma and F. Izumi, J. Appl. Crystallogr. **44**, 1272 (2011).
[48] Depending on the chosen fitting range to fit the Curie-Weiss law, a variation in the values of Θ and μ_{eff} was observed as a result of varying temperature independent susceptibility (χ_0).
[49] M. Bouvier, P. Lethuillier, and D. Schmitt, Phys. Rev. B **43**, 13137 (1991).
[50] C. Kittel, *Introduction to Solid State Physics*, 7th ed.(John Wiley & Sons, Singapore, 1996).
[51] N. D. Mermin and H. Wagner, Phys. Rev. Lett. **17**, 1133 (1966).
[52] R. Kumar, Tusharkanti Dey, P. M. Ette, K. Ramesha, Atasi Chakraborty, I. Dasgupta, R. Eremina, S. Tóth, A. Shahee, S. Kundu, M. Prinz-Zwick, A. A. Gippius, H. A. Krug von Nidda, N. Büttgen, P. Gegenwart, and A. V. Mahajan, Phys. Rev. B **99**, 144429 (2019).
[53] H. J. Xiang, E. J. Kan, S.-H. Wei, M.-H. Whangbo, and X. G. Gong, Phys. Rev. B **84**, 224429 (2011).
[54] L. Messio, C. Lhuillier, and G. Misguich, Phys. Rev. B **83**, 184401 (2011).
[55] Below a field of 3 T, ^{31}P-NMR measurements attempt remained unsuccessful because of the low-frequency ringing issue. We did see two distinct NMR lines at room temperature while

measuring the ^{31}P-NMR spectrum at a magnetic field of strength ∼13 T.
[56] T. Moriya, Phys. Rev. **101**, 1435 (1956).
[57] R. Orbach, Proc. R. Soc. London A **264**, 458 (1961).
[58] M. Evangelisti, F. Luis, L. J. de Jongh, and M. Affronte, J. Mater. Chem. **16**, 2534 (2006).
[59] At high temperatures, there is a large uncertainty in determining the magnetic specific heat as the specific heat is mainly dominated by the lattice contribution, thus the Schottky fit deviates from the experimental data. In order to minimize the error in determining the Schottky gap, especially at the higher temperature side, we also estimated the gap using another nonmagnetic analogue, $Li_9Ga_3(P_2O_7)_3(PO_4)_2$ (LGPO), and the error in gap size was chosen by comparing the absolute error resulted in $\frac{\Delta_S}{k_B}$ by using LAPO and LGPO. We then used this result to compare with the NMR gap size.